# The problematic $\psi_1$ ocean tide

R.D. Ray [1], J.-P. Boy [2], B.K. Arbic,[3] G.D. Egbert [4], S.Y. Erofeeva,[4] L. Petrov[1] and J.F. Shriver[5]

[1]*Geodesy & Geophysics Laboratory, NASA Goddard Space Flight Center, Greenbelt, MD* 20771, *USA. E-mail: richard.ray@nasa.gov*
[2]*CNRS, Université de Strasbourg, Strasbourg, France*
[3]*Department Earth & Environmental Sciences, University of Michigan, Ann Arbor, MI* 48109, *USA*
[4]*College of Earth, Ocean, & Atmospheric Sciences, Oregon State University, Corvallis, OR* 97331, *USA*
[5]*Naval Research Lab, Stennis Space Center, MS* 39529, *USA*

## SUMMARY

Observations of the $\psi_1$ earth tide yield valuable insights into the earth's free core nutation, especially if the effects of the $\psi_1$ ocean tide can be removed. The ocean tide is extremely small, with amplitudes rarely more than a few millimetres, and developing an accurate model is challenging. Direct observations are inadequate to support a global model. The alternative—numerical simulation—must account for a multitude of possible effects. The ocean tide is forced by the gravitational tidal potential, by pressure loading from atmospheric tides, by seasonal modulation of the nearby $K_1$ constituent, and possibly by non-linear interactions among several other constituents. Here we construct a model of the $\psi_1$ ocean tide which accounts for (or attempts to bound) each of these effects. The radiational component (from atmospheric pressure loading), although relatively small, is complicated by the presence of non-tidal atmospheric variability in the diurnal band. The ocean's response is dynamic, but there is also high-wavenumber pressure forcing with a near-isostatic response. A general circulation model, forced by both winds and the tidal potential, suggests that annual variability in $K_1$ leads to pronounced $\psi_1$ amplitudes in some marginal seas, especially in the western Pacific.

**Key words:** Loading of the Earth; Tides and planetary waves.

## 1 INTRODUCTION

The geophysical importance of the $\psi_1$ tide is out of all proportion to its tiny size. The $\psi_1$ ocean tide is rarely more than a few mm anywhere in the global ocean; the $\psi_1$ earth tide has a maximum amplitude, at latitudes $\pm45°$, of only 1.2 mm. That such a tiny tide can be important is due solely to an accident of geophysics: the $\psi_1$ frequency falls very close to that of the nearly diurnal free wobble (NDFW), one of the resonant free modes of the earth's rotation (Dehant & Mathews 2015). The resonance causes a large perturbation in the magnitude of the $\psi_1$ earth tide—see Fig. 1—thus making measurements of $\psi_1$ an ideal way to explore characteristics of the rotational mode. Since the resonant frequency is determined by the size and ellipticity of the core, its proximity to $\psi_1$ is mere chance. In fact, in light of changes in the planetary rotation rate and in the shape of the core–mantle boundary over time, it appears likely that the NDFW resonance once coincided with the frequency of $\psi_1$ (Toomre 1974; Greff-Lefftz & Legros 1999) and, farther back in time, with the constituent $\phi_1$; possible geological consequences of the magnified resonant responses were explored by Greff-Lefftz & Legros (1999).

Important studies of the NDFW, or the associated free core nutation (FCN), which have been based on analysis of diurnal earth tides include: Neuberg *et al.* (1987), Merriam (1994), Ducarme *et al.* (2007), Rosat *et al.* (2009) among others. For these kinds of investigations, $\psi_1$ usually provides an important constraint, even with its very small amplitude. Cui *et al.* (2018), in fact, stress the sensitivities in their estimated resonance parameters to $\psi_1$. But to isolate the earth-tide resonance it is necessary that ocean-tide effects be removed from the observed $\psi_1$ earth-tide signal. For gravimetry the ocean effects include both the Newtonian attraction of the ocean mass and the associated effects of crustal loading and deformation. Thus, the geophysical community has a longstanding need for an acceptably accurate model of the $\psi_1$ ocean tide, but the pathway to such a model is plagued with difficulties.

Owing to its small size, direct measurements of the $\psi_1$ ocean tide must contend with an unfavorably small signal-to-noise ratio. Estimates from tide-gauge data can have large uncertainties and also tend to be somewhat unstable, either from noise contamination or from vagaries in the non-gravitational forcing at nearby frequencies, as discussed further below. Use of Topex/Poseidon and Jason satellite altimetry, which has been so valuable in determining most

major tides (e.g. Le Provost 2001), is hindered by a relatively long alias period for $\psi_1$ of 329 d (Ray & Egbert 2018, fig. 13.2), which is uncomfortably close to the annual cycle with its large and broadband variability. This leads to altimeter estimates of $\psi_1$ that are dominated by noise. It seems that determining the $\psi_1$ ocean tide must rely on more indirect methods, notably numerical simulations, but these too are unusually complicated because of the different physical mechanisms that come into play for such a small tide.

The various physical mechanisms generating $\psi_1$ in the ocean are addressed below in detail, but a brief summary is as follows:

(i) *Gravitational*. The astronomical tidal potential, as one might expect, accounts for a significant part of the $\psi_1$ ocean tide, although not always the largest part everywhere. Perturbations from the body tide require knowledge of the Love number combination $\gamma_2$ which, as Fig. 1 emphasizes, is anomalous and in fact is typically the object of the investigation.

(ii) *Radiational*. Part of $\psi_1$ is forced by pressure loading from the $\psi_1$ atmospheric tide. This tide is a manifestation of semiannual variability in the much larger $S_1$ atmospheric tide. As the $S_1$ air tide is somewhat variable in time (e.g. Vial *et al.* 1994; Schindelegger *et al.* 2017), its semiannual modulation is also variable. More importantly, it can be overwhelmed by non-tidal background variability.

(iii) *Seasonality*. Because the frequency of $\psi_1$ is separated by 1 cycle per year (cpy) from the frequency of the large $K_1$ constituent, seasonal perturbations in the latter, caused by seasonal changes in the ocean, can affect, or even dominate, $\psi_1$. An impressive example, at New Westminster, Canada, is discussed below.

(iv) *Non-linearity*. Several potential compound tides exist at the $\psi_1$ frequency. We suspect these are very small, because in all cases at least one of the interaction constituents is small. An example is $KS_1$, from interaction between $K_2$ and $S_1$.

In summary, the problematic nature of $\psi_1$ stems from both its tiny size and from all the different ways it can be generated. Each of the mechanisms is discussed in a separate section below as we attempt to construct a global representation of $\psi_1$. The goal is to arrive at an approximate global chart of $\psi_1$ amplitudes and phases which can be used in geophysical studies of the NDFW resonance. Perhaps more important is to understand the potentially large errors in any such global chart. Sections 2, 3, 4 and 5 discuss in turn the various components that combine to form $\psi_1$. The modelled tide is briefly compared with bottom pressure measurements in Section 6. The implied $\psi_1$ load-tide corrections to gravimetry are examined in Section 7.

## 2 THE GRAVITATIONAL COMPONENT OF $\psi_1$

In the astronomical tidal potential, $\psi_1$ originates as a modulation of the large $K_1$ constituent caused by the ellipticity of the earth's orbit. The varying earth–sun distance induces an annual modulation in the solar part of $K_1$, and $\psi_1$ is one of the modulating sidelines. (The other sideline is one of the couplet of lines that forms $S_1$.) Since the tidal potential is maximum as earth passes perihelion, the modulation is once per anomalistic year (from one perihelion to the next), and the tidal arguments of $\psi_1$ and $K_1$ must differ by $\ell'$, the earth's mean anomaly. The earth's orbital ellipticity is relatively small, so the resulting $\psi_1$ tide is also small (as is the gravitational part of $S_1$).

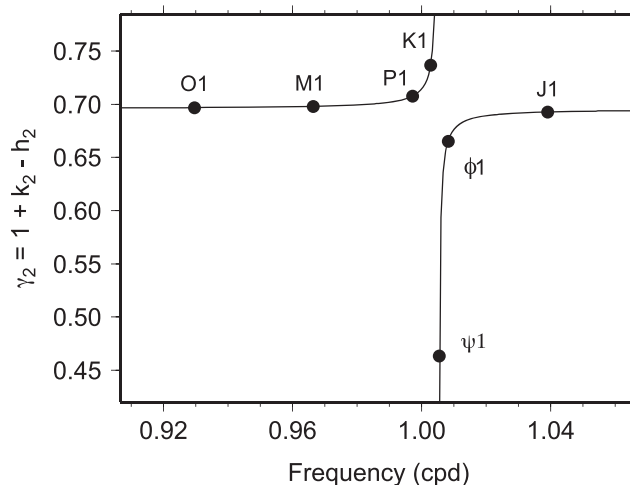The conventional tidal arguments for $K_1$ and $\psi_1$ are written (Pugh & Woodworth 2014):



**Figure 1.** The Love number combination $\gamma_2 = 1 + k_2 - h_2$ across the diurnal tidal band. The nearly diurnal free wobble (NDFW) resonance, sitting between constituents $K_1$ and $\psi_1$ at approximate frequency 1.005067 cpd is evident; the resonance affects primarily $\psi_1$. Displayed values of $\gamma_2$ are taken from Mathews *et al.* (1995); the solid line follows their eq. (35).

$$\Theta_K(t) = \tau + s + \pi/2 = T + h + \pi/2 \qquad (1)$$

$$\Theta_\psi(t) = \tau + s + h - p_s + \pi/2 = T + 2h - p_s + \pi/2, \qquad (2)$$

where $\tau$ is mean lunar time, $T$ is mean solar time and $s$, $h$, $p_s$ are the mean longitudes of the moon, the sun, and the sun's perihelion, respectively, reckoned relative to the spring equinox. Note that $\ell' = h - p_s$, so the two arguments indeed differ by $\ell'$. The shorthand Doodson numbers for the two constituents are 165.555 for $K_1$ and 166.554 for $\psi_1$. The $\pi/2$ offsets in both arguments arise from adopting a cosine functional form for tidal oscillations, which is standard, when the astronomical potential for these particular constituents requires sine functions (Cartwright & Tayler 1971).

If desired, the astronomical longitudes may be eliminated in (2) by inserting standard polynomial expansions (Meeus 1998) and simplifying. The result for the $\psi_1$ argument is

$$\Theta_\psi(t) = 3.276489 + 7.31202554 \cdot 10^{-5}(t - t_0) \qquad (3)$$

in radians, where $(t - t_0)$ is the time in seconds of UT1 since epoch J2000.

The frequency of the $K_1$ tide is 1 cycle per sidereal day, or 1.0027379 cycles per solar day (cpd), or 15.041069° hr$^{-1}$. Adding 1 cycle per anomalistic year places the frequency of $\psi_1$ at 1.0054757 cpd or 15.082135° hr$^{-1}$. These frequencies can, of course, be determined from the rates of the fundamental arguments given in eq. (2). Other neighboring tidal constituents, which together form the $K_1$ group, are shown in Fig. 2.

Because its frequency is so close to that of the major constituent $K_1$, the amplitude and phase of the gravitational part of the $\psi_1$ ocean tide at any location is probably best determined by inference (Pugh & Woodworth 2014). The phase lag $G$ may be set identically to that of $K_1$, and the amplitude $H$ may be scaled by the relative amplitudes in the potential. One must also account for perturbations induced by the body tide, which is normally handled by scaling the tidal potential by the Love number combination $\gamma_2 = 1 + k_2 - h_2$, as shown in Fig. 1. We use the diurnal Love numbers derived by Mathews *et al.* (1995). Thus, $\gamma_2 = 0.7365$ for $K_1$ and 0.4631 for $\psi_1$. For further details on diurnal-band tidal inference, see Ray (2017).
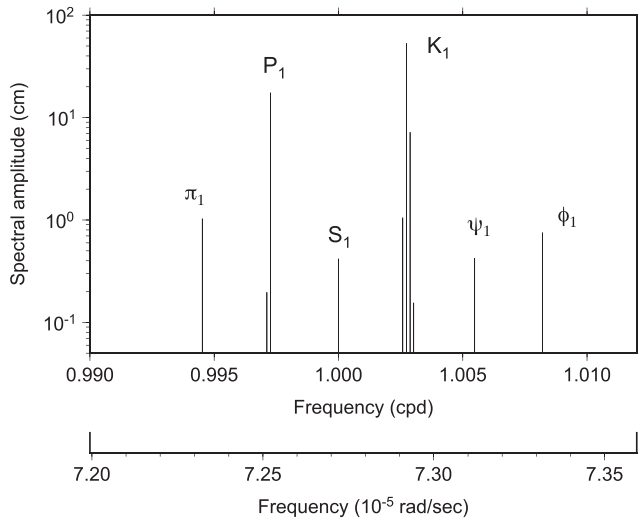
**Figure 2.** Spectral lines of the astronomical tide-generating potential within the $K_1$ tidal group. Amplitudes are according to Table 1b of Cartwright & Edden ([1973](#)).

For $K_1$ we adopt the global inverse solution TPXO.8, one of the series of hydrodynamic models constrained by many years of satellite altimetry (Egbert & Erofeeva [2002](#)). The inferred $\psi_1$ cotidal chart is shown in Fig. [3](#).

The errors in Fig. [3](#) arise either from errors in the underlying $K_1$ or from errors in our adopted Love numbers—for example, if the FCN frequency used by Mathews *et al.* ([1995](#)) is in error. A quality assessment of TPXO.8 is included in the review by Stammer *et al.* ([2014](#)); it is one of the best global models now available. Comparison against deep-ocean bottom pressure measurements of $K_1$ gives an RMS difference of only 0.44 cm. But like all present-day models, it has relatively large errors in polar regions, especially under Antarctic ice shelves (e.g. fig. 9 of Stammer *et al.* ([2014](#))).

What of errors in adopted Love numbers? The Love numbers of Mathews *et al.* ([1995](#)) are based on a FCN period of 429.6 d, which is close to the observed values commonly reported (Herring *et al.* [1986](#); Rosat *et al.* [2009](#)), although Chao & Hsieh ([2015](#)) recently estimated the period at 440 d. The theoretical value, based on a hydrostatic Earth model, is about 460 d (Wahr [1981](#)). The FCN period of 460 d would significantly modify $\gamma_2$ for $\psi_1$, yielding approximately 0.528 rather than 0.463; the value for $K_1$ would be hardly affected. Thus, if the Love numbers of Mathews *et al.* ([1995](#)) were in error by this amount—which is not expected—the amplitudes of our inferred $\psi_1$ gravitational ocean tide in Fig. [3](#) would be too small by a factor of 0.88. Additional possible errors, stemming from inadequate modelling of mantle anelasticity or core-mantle coupling, are thought to generate smaller perturbations (Mathews *et al.* [2002](#)).

## 3 THE RADIATIONAL COMPONENT OF $\psi_1$

Determining the radiational component of the $\psi_1$ ocean tide—that is the component caused by pressure forcing by the atmospheric tide—is more difficult. There is no recourse but to numerical simulation via a properly tuned numerical ocean model. The model must be forced by the $\psi_1$ atmospheric tide, to which we now turn.

### 3.1 The $\psi_1$ air tide

Because we require an atmospheric barometric tide over the entire global ocean, we can hardly rely on relatively sparse barometric station data, but must instead use numerical general circulation models. This has been a standard approach for many years now (Zwiers & Hamilton [1986](#)), and many studies have compared the atmospheric tidal signals among models and against station data (e.g. Dai & Wang [1999](#); Covey *et al.* [2014](#); Schindelegger & Ray [2014](#)). Comparisons have been made for $S_1$ and for other major atmospheric tidal frequencies, including seasonal decompositions, although not explicitly for the small $\psi_1$—which we recall represents a semiannual modulation of $S_1$.

We have determined the diurnal atmospheric tides from two meteorological reanalysis products: the European Centre for Medium-Range Weather Forecasts (ECMWF) ERA5 (Hersbach *et al.* [2020](#)) and Modern-Era Retrospective Analysis for Research and Applications, version 2 (MERRA-2), produced by the NASA Global Modeling and Assimilation Office (Gelaro *et al.* [2017](#)). Both reanalyses distribute hourly surface pressures over the whole globe. We analysed ERA5 data over the period 2000–2017 and MERRA2 data over 1980–2017.

The extracted $S_1$ and $\psi_1$ tides are shown (amplitudes only) in Fig. [4](#). The $S_1$ amplitudes agree qualitatively with each other and with other previously published depictions of the tide (e.g. Schindelegger & Ray [2014](#)). The largest signals, forced primarily by boundary layer heating, occur over large land masses. The tides are generally smaller over the oceans, although amplitudes still exceed 50 Pa in many regions.

The agreement in $\psi_1$ between ERA5 and MERRA2 is not too unreasonable over the tropical oceans, given the small amplitudes, but outside the tropics the agreement is poor. In fact, both results take on a high-wavenumber, noise-like character outside the tropics. Whether these $\psi_1$ estimates are legitimate signal or mere noise becomes evident by examining time series spectra at individual locations. Two examples for ERA5 pressure data are shown in Fig. [5](#). At a location in the tropical South Atlantic (top panel), the $\psi_1$ peak is small but clearly defined, and it sits well above the background. In contrast, at a location over the South Atlantic at latitude 60° S (lower panel), the background variability is much higher and no tidal peak can be seen, even at $S_1$.

The dependence on latitude and background noise is brought out more clearly in Fig. [6](#) which shows ERA5 pressure spectra along a complete meridian, 170°W, and extended over the wider frequency range of 0–3 cpd. The generally 'quiet' atmosphere of the tropics is evident, and this facilitates detection of small tidal signals there. Pressure variability increases by orders of magnitude once outside the tropics, although decaying at higher frequencies. Thus, the semidiurnal $S_2$ and terdiurnal $S_3$ are above background at all latitudes, but $S_1$—let alone $\psi_1$—becomes difficult to extract from background noise at latitudes polewards of about 40°. From Figs [5](#) and [6](#) we conclude that the reanalysis-based $\psi_1$ tide charts of Fig. [4](#) contain legitimate signals over the tropics, be they accurate or inaccurate, but elsewhere the $\psi_1$ charts mostly represent non-tidal atmospheric variability.

### 3.2 Oceanic response to $\psi_1$ air tide

To develop a model of the radiational component of the $\psi_1$ ocean tide, we have used the $\psi_1$ atmospheric tide, as represented in the ERA5 reanalysis (Fig. [4](#), lower left-hand panel), to force a numerical ocean model. This was done in the frequency domain by
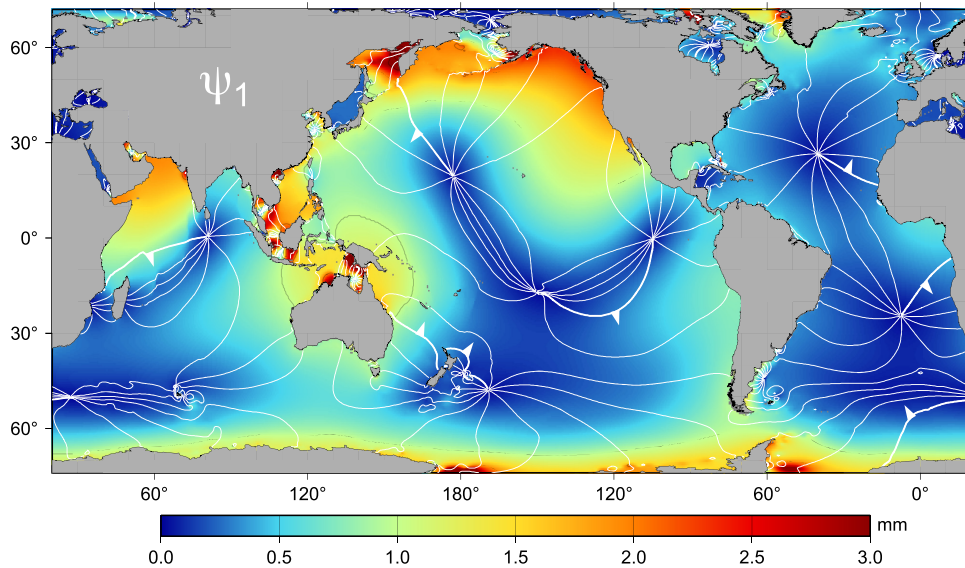
**Figure 3.** Cotidal chart of the gravitational component of the $\psi_1$ ocean tide, as determined by inference from the nearby $K_1$. Inference accounts for the variation in diurnal-band Love numbers, which are adopted from Mathews *et al.* (1995); see Ray (2017) for a discussion of inference within the diurnal band and how it is affected by the core resonance. Thickest phase lines denote $0°$, with small arrows giving sense of propagation direction.
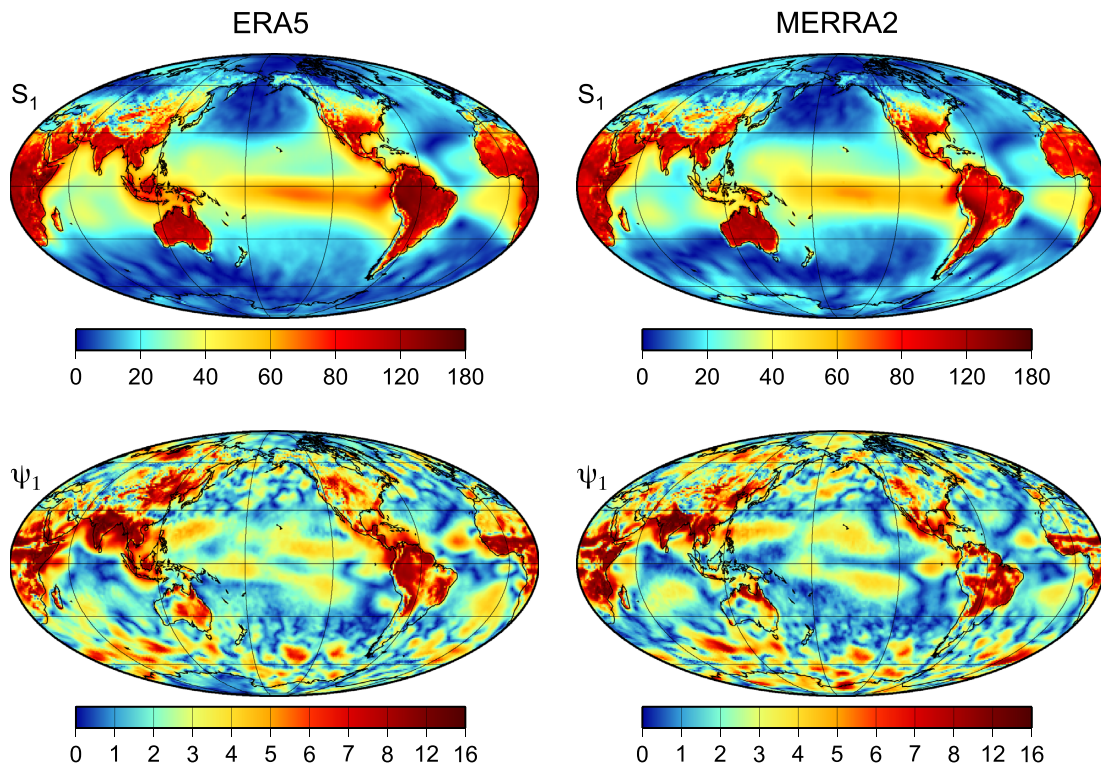


**Figure 4.** Amplitudes (Pa) of the (top panel) $S_1$ and (bottom panel) $\psi_1$ atmospheric tides in barometric surface pressure, from multiyear tidal analyses of meteorological reanalysis products (left-hand panel) ERA5 and (right-hand panel) MERRA2.

factoring the coefficient matrix for a finite-difference discretization of the wave equation derived from the shallow-water equations (Egbert & Erofeeva 2002). Dissipation was linearized, with a 'friction velocity' set to $1\,\mathrm{m\,s^{-1}}$, a value that was used for other diurnal constituents in the development of the TPXO.8 atlas. Forcing from self-attraction and loading was here ignored, since it is difficult to justify the additional calculations when the uncertainties in the air-tide forcing are so large. (We similarly ignored the effects of attraction and loading from the air tide.) As a rough guide to the expected level of errors in the hydrodynamic model, one might consider the TPXO.8 diurnal constituents, where differences between the prior hydrodynamic and the final inverse solutions are, as a global average, of order 30 per cent. Of course, for those waves the forcing is known perfectly, whereas in the present case the forcing—the $\psi_1$ air tide—has its own substantial uncertainties.
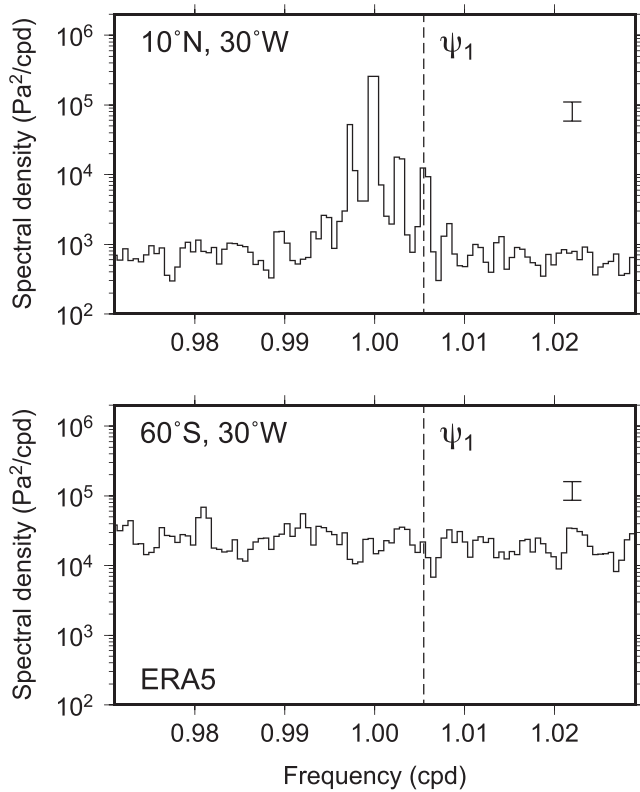
**Figure 5.** Spectrum of barometric pressure from ERA5 reanalysis, at two locations: (top) latitude 10°N where background noise is relatively low and (bottom) latitude 60°S where background noise is high. Spectra were calculated from hourly data over 2000–2017. Error bar represents a 95 per cent confidence interval for an isolated spectral peak relative to background, following Percival & Walden (1993, p. 300).

The computed ocean response to the ERA5 air tide is shown in Fig. 7(a) (only amplitudes are shown, as the phases are rather erratic over much of the ocean owing to the small amplitudes). The response in the Pacific is especially small, with amplitudes of only 1 mm or smaller nearly everywhere. Parts of the Atlantic and especially the Indian Ocean experience larger responses, although still small in absolute terms. The largest amplitudes, between 2 and 3 mm, are in the South China Sea. The high-wavenumber noise-like features evident in the air-tide forcing are also evident in the ocean response, especially throughout the Southern Ocean.

How much of the ocean response seen in Fig. 7(a) is an isostatic, nearly inverted-barometer response to the air tide? It is well known that at periods shorter than about 2 d the inverted-barometer description of the ocean's response tends to fail (e.g. Wunsch 1972). For any given load, the response is a complicated function of bottom topography, the zonal and meridional wavenumbers of the forcing, and the frequency of the forcing relative to the Coriolis parameter (Wunsch & Stammer 1997). In the global barotropic model of Ponte *et al.* (1991), zonal wavenumbers higher than about $2\pi/(5000 \text{ km})$ tend towards an inverted-barometer response, even at relatively high (but still subdiurnal) frequencies. The high-wavenumber 'noise' in Fig. 7(a) may well be a simple isostatic response of the ocean to high-wavenumber forcing.

To confirm this, we have combined the computed ocean tide of Fig. 7(a) with the atmospheric tide of Fig. 4 to form essentially a combined bottom pressure (in equivalent height units), shown in Fig. 7(b). The noise-like features are indeed mostly eliminated and

we are left with the ocean's relatively long-wavelength dynamic response to the air tide. Some of this response calls to mind features typical of diurnal gravitational tides (*cf.* Fig. 3), such as the larger amplitudes in the Indian Ocean as well as the hint of an Antarctic Kelvin wave, although there is little indication of high amplitudes in the North Pacific. Resonances in the South China Sea and the Gulf of Mexico are also common in gravitational tides. In fact, resonances in these locations are found in a number of barotropic normal modes of the near-diurnal band, according to Müller (2009), so it is unsurprising that they can be resonantly excited by the $\psi_1$ air tide.

Because of the cusp-like features apparent in the diurnal-band pressure spectrum (Fig. 5, top), there is variability in atmospheric tides in addition to that represented by seasonal sidelines (e.g. Schindelegger *et al.* 2017). Similarly there must be some temporal variability present in both panels of Fig. 7, and the corrections needed for gravimeter data will depend to some extent on the time period over which the gravity data were collected. This suggests an alternative approach to handling radiational ocean-tide effects for gravimetry and similar applications. Standard processing of gravimetric earth-tide data (Boy 2019) already requires removal of atmospheric mass effects via integration of the global pressure fields extracted from atmospheric analysis or reanalysis products, nowadays often at hourly time resolution. Typically an inverted-barometer response is used for the pressures over ocean regions. An alternative would be to drop the inverted barometer assumption in such calculations and instead allow the barometric pressures to force a numerical ocean model, the output of which will automatically include radiational tides, whether their response is inverted barometer or not. The radiational ocean tide effects will then automatically be included with the atmospheric mass corrections. These signals will correspond as closely as possible to actual pressures occurring over the oceans during the same time as the geodetic measurements are collected. There will be no need to assume a time-invariant fixed air tide, as in our Figs 4 and 7.

An example of such a numerical ocean model forced by either operational or reanalysis meteorological data is the Toulouse Unstructured Grid Ocean model (T-UGOm, Florent Lyard, personal communication, 2020), which follows earlier work described by Carrère & Lyard (2003). There are, of course, other ocean models that could be used. A complication is to ensure that radiational effects in other tidal constituents (e.g. $K_1$) are not double-counted. Carrère *et al.* (2016) discusses some aspects of this complication.

## 4 $\psi_1$ AS SEASONAL SIDELINE TO $K_1$

In coastal waters it is not uncommon to observe seasonal perturbations in a large constituent like $M_2$ (e.g. Corkan 1934; Cartwright 1968; Amin 1982; Huess & Andersen 2001), especially in polar regions where seasonal ice cover impacts tidal dynamics (e.g. Prinsenberg 1988). Similar perturbations have been observed in some deeper parts of the ocean, likely the result of seasonal perturbations in ocean stratification (Kang *et al.* 2002).

Seasonal variations in the large diurnal $K_1$ constituent would be manifested by energy in $S_1$ and $\psi_1$, each 1 cpy from $K_1$. Given the small amplitude of the $\psi_1$ gravitational tide, we expect this $K_1$-modulation effect could well be a dominant mechanism for exciting $\psi_1$ in some places. In fact, of the many tide gauges we have had occasion to examine, the largest $\psi_1$ tide that we have ecountered is almost certainly due to this effect. The gauge is at New Westminster, near Vancouver, Canada, and sits near the mouth, but well within,
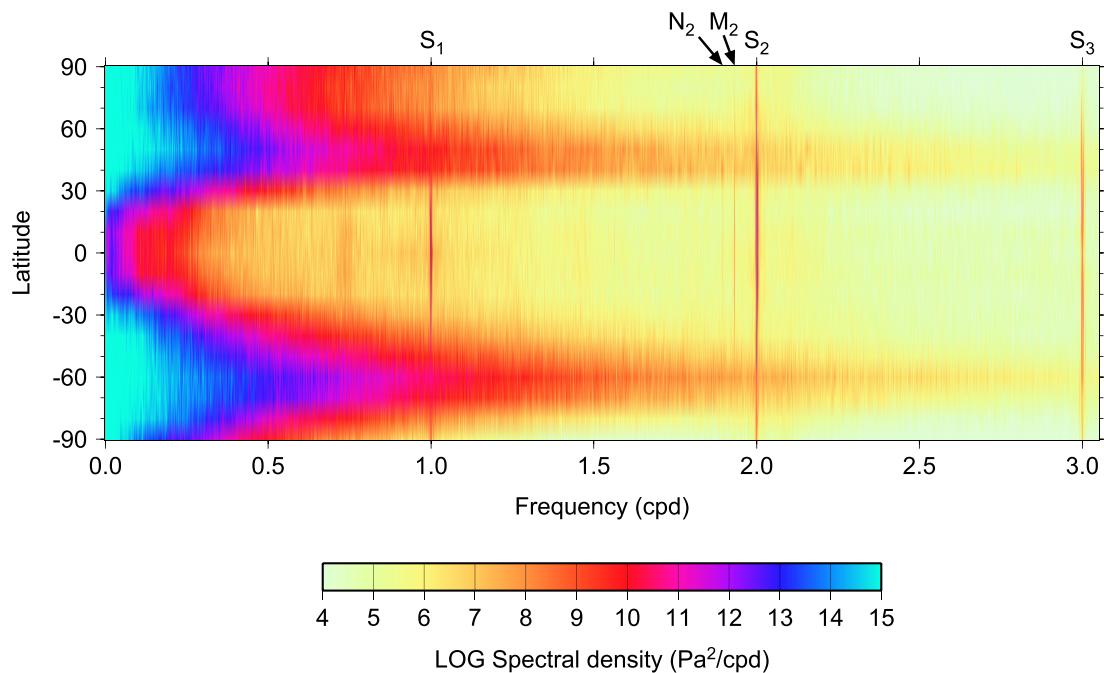
**Figure 6.** Spectra of ERA5 surface pressures, as function of frequency (horizontal axis) and latitude (vertical axis), along the 170°W meridian. Based on ERA5 hourly pressures over 2000–2017. Main thermal tides, $S_1$ through $S_3$ are labelled at top; they show up clearly against non-tidal background variability, although $S_1$ can possibly be masked by high noise in the 50°–60° latitude band. A faint line from the lunar $M_2$ tide is apparent, to the left of $S_2$, and an even fainter line from the lunar elliptic tide $N_2$ (Malin & Chapman 1970; Matsuno 1980) is barely apparent left of $M_2$. A broad low-latitude feature at approximately 0.75 cpd is presumably the signature of a free atmospheric normal mode—a Kelvin wave of period 33 hr (Hamilton & Garcia 1986; Matthews & Madden 2000). Colour scale saturates at low and high spectral levels.

the Fraser River. Analysis of the New Westminster tide gauge data yields a $\psi_1$ amplitude of 54 mm. Because $O_1$ and $M_2$ have large seasonal sidelines there (see Fig. 8), the large $\psi_1$ is surely caused by similar seasonality in $K_1$. One suspects the seasonal changes are related to river discharge, so the large tide is likely very localized and of no great importance to gravimetric geodesy. Cummins *et al.* (2000) reported large seasonal changes in diurnal tidal currents on the oceanward side of Vancouver Island, caused by freshwater influences on stratification, but these are likely associated with shelf waves with little elevation signature.

A global view of seasonal perturbations of $M_2$ was first published by Müller *et al.* (2014), who analyzed the output of a high-resolution ocean model forced by both the atmosphere and the tidal potential, including an embedded sea-ice model. Their atmospheric forcing was based on climatological winds; the tidal forcing was based on a full tidal spectrum evaluated directly from an accurate lunar and solar ephemeris.

In this section we report on a similar exercise in order to clarify to what extent $\psi_1$ may be partially a manifestation of the seasonal modulation of the $K_1$ constituent. We used the Hybrid Coordinate Ocean Model (HYCOM), developed at the U.S. Naval Research Laboratory. We used a 5-yr simulation, which was run on a grid with nominal horizontal grid spacing of $(1/12.5)°$ and 32 hybrid layers in the vertical. The simulation was forced by 3-hourly atmospheric fields from the Fleet Numerical Meteorology and Oceanography Center, with wind speeds scaled to be consistent with QuikSCAT observations. Note that atmospheric surface-pressure loading was *not* modelled, so there are no radiational tides generated, other than those produced, for example, by daily sea breeze along continental coastlines (e.g. Álvarez *et al.* 2003). The HYCOM simulation used a parametrized topographic wave drag, meant to stand in for breaking

of unresolved high-vertical-mode internal tides, as first described by Arbic *et al.* (2010). This same 5-yr HYCOM run has been previously used by Shriver *et al.* (2012), Nelson *et al.* (2019) and others, although for purposes different from ours here. Shriver *et al.* assessed the quality of the simulated $K_1$ constituent by comparing against an altimeter-constrained model; they found an RMS error of 2.25 cm, which is comparable to errors seen in other forward unconstrained models, and much smaller than the $\sim$9.5 cm area-weighted deep-water $K_1$ signal.

Unlike Müller *et al.* (2014) who used the complete tidal potential via an ephemeris, our HYCOM simulation used a tidal potential consisting of only 8 pure harmonics (the 4 largest diurnal and semdiurnal constituents). The simpler HYCOM forcing is ideal for the present work, because then any model energy generated at the $\psi_1$ frequency will arise neither from direct gravitational nor atmospheric-pressure forcing, allowing us to avoid double-counting mechanisms already discussed above.

The result is shown in Fig. 9. Throughout most of the deep open ocean the amplitudes are much smaller than the gravitational component of $\psi_1$, as depicted in Fig. 3. The opposite, however, occurs in many marginal seas, especially those in the western Pacific. In the Yellow and Okhotsk Seas, the Gulf of Tonkin, the western South China Sea and along the coast of northern Australia, the amplitudes exceed 10 mm. These are all locations of large $K_1$ tides, so a large $\psi_1$ is not surprising so long as sufficiently large seasonal changes in the ocean occur. It is also possible that some of these marginal seas could be reflecting modulations of daily wind-stress forcing of the sort described by Álvarez *et al.* (2003).

Is there *in situ* evidence for any of the large seasonal tide features in the HYCOM simulation? We have not attempted a thorough assessment, but we give one example. (Section 6 below also examines
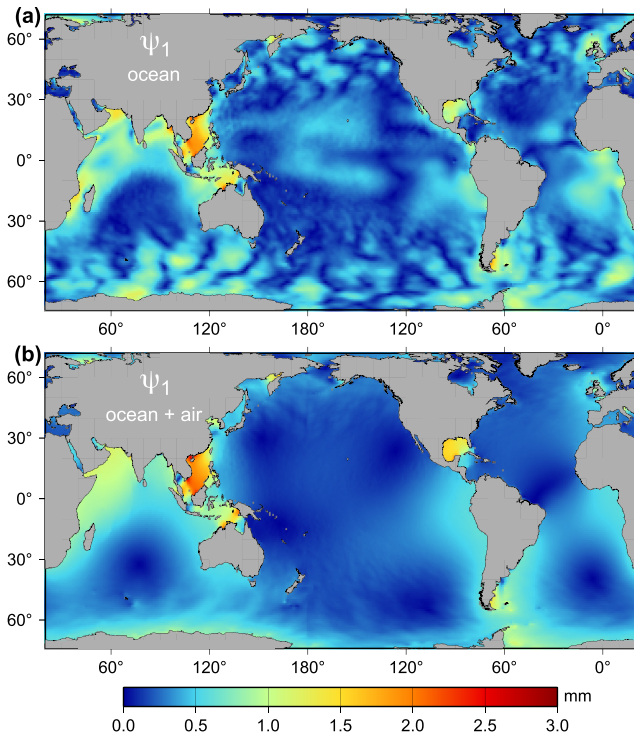
**Figure 7.** (a) Amplitudes (mm) of the radiational component of the $\psi_1$ ocean tide, computed by solving a frequency-domain wave equation as forced by pressure loading from the $\psi_1$ atmospheric tide. (b) Amplitudes (in mm of equivalent ocean height) of the $\psi_1$ combined ocean and atmospheric bottom pressure. The panel thus depicts the ocean's dynamic response to the $\psi_1$ atmospheric tide. The high-wavenumber noise-like features of panel (a) are mostly eliminated in (b), thus indicating that they are primarily an inverted barometer response to the non-tidal noise-like features of the air tide (Fig. 4), which therefore disappear in bottom pressure.

*in situ* comparisons, but only for the deep ocean where the HYCOM results for $\psi_1$ are small.) Fig. 10, focusing on the Yellow and East China Seas, shows the HYCOM annual sidelines of $K_1$ (top panels) and $O_1$ (bottom panel). Tide gauge measurements cannot be used to assess the former, because other components are in play (such as the gravitational components discussed earlier), but they can be used to assess the $O_1$ results. The $O_1$ sideline, dubbed here $OB_1$, appears strikingly similar to $\psi_1$, but $S_1$ is larger than the other components in the north, reaching amplitudes exceeding 40 mm, possibly from diurnal wind effects. (Recall there was no surface pressure forcing in this HYCOM simulation.) Table 1 compares HYCOM and tide-gauge estimates of the amplitides and phases of $OB_1$ at five tide gauges along the coast of China (locations shown in lower right-hand panel of Fig. 10; we computed these tide-gauge estimates from multiyear time-series of hourly data).

One cannot expect perfect agreement from a model unconstrained by observations, but Table 1 does show that HYCOM amplitudes are roughly comparable with the *in situ* data, and the phases are in the correct quadrant, and sometimes better than that. Based on this, we are led to conclude that the HYCOM simulation is probably yielding a realistic first look at the possible seasonal modulations of $K_1$ throughout the global ocean. The large $\psi_1$ amplitudes along the western Pacific marginal seas are likely to be particularly significant for geodetic studies of the $\psi_1$ earth tide in that region.

## 5 NON-LINEAR COMPONENT

It is conceivable that a component of the $\psi_1$ ocean tide arises from non-linear interactions between other constituents. Several combinations are possible: interaction between $R_2$ and $P_1$, generating a nominal compound $RP_1$ tide; interaction between $K_2$ and $S_1$, generating a nominal compound $KS_1$ tide. The latter could also be produced by triple interaction of twice $K_1$ with $S_1$. Our HYCOM simulations are uninformative of these interactions because relevant constituents were excluded. Moreover, including them would have required modelling atmospheric loading from surface air pressures, because the $S_1$ constituent is mostly of radiational origin (Ray & Egbert 2004), as is a substantial fraction of $R_2$ (from seasonal modulations of the $S_2$ atmospheric tide).

The compound tides $RP_1$ and $KS_1$ are expected to be small, since experience shows both $R_2$ and $S_1$ to be less than a few cm at almost all locations. Our HYCOM simulations may, however, allow some reasonable upper bounds to be set.

The compound $KS_1$ is probably everywhere smaller than the compound $KQ_1$, representing interaction between $K_2$ and $Q_1$, because $Q_1$ is invariably larger than $S_1$. In terms of their global means, the amplitude of $Q_1$ is approximately 1.8 cm, and $S_1$ is 0.5 cm. In the HYCOM simulation, $KQ_1$ (with frequency identical to the linear $\upsilon_1$) is everywhere smaller than 1 mm, except for a few isolated locations, the largest being in the Gulf of Thailand where it reaches about 5 mm. We thus expect $KS_1$ to be less than 2 mm there, which is smaller than the amplitudes seen at that location in Figs 3 or 9. It must be less than 1 mm nearly everywhere else. $KS_1$ is therefore probably an insignificant contributor to the oceanic $\psi_1$.

By similar logic, we expect the compound $RP_1$ to be much smaller than $NP_1$, because the linear $N_2$ tide dominates $R_2$ everywhere, often by two orders of magnitude or more. In the HYCOM simulation, we found that $NP_1$ is less than 0.5 mm everywhere except again at a few isolated locations. The largest amplitude is in the upper Sea of Okhotsk, where it reaches nearly 9 mm. If $RP_1$ is two orders of magnitude smaller, then its contribution to the $\psi_1$ tide is insignificant.

## 6 COMPARISONS WITH BOTTOM PRESSURE STATIONS

We now have three separate models representing different physical effects that can contribute to the observed $\psi_1$ tide in the ocean. As a rough guide to assess how realistic the developed model components are, it is useful to compare with reliable *in situ* tidal measurements. Fig. 10 is no more than a suggestion that the magnitude of the $K_1$ annual modulation along the coast of China is about right. Here we compare the modelled $\psi_1$ with direct measurements made by bottom pressure recorders sitting on the seafloor. This database of tidal constants was compiled a few years ago (Ray 2013) and was used extensively in the study of Stammer *et al.* (2014). There are 151 stations in the database, of which 114 include the $\psi_1$ constituent. All stations are located in deep water, so these tests will not assess the very largest amplitudes that evidently occur along the western margins of the Pacific. Moreover, roughly half are in the Atlantic, where the $\psi_1$ tide is weak, so the test data set is not ideal.

The bottom pressures are sensitive to both the $\psi_1$ ocean tide and atmospheric tide. Thus, for the radiational component of $\psi_1$, we use the data shown in Fig. 7b, which includes the atmospheric pressure.

The comparison statistics are tabulated in Table 2. The total RMS signal of $\psi_1$ in the bottom pressure stations is 1.15 mm, very small
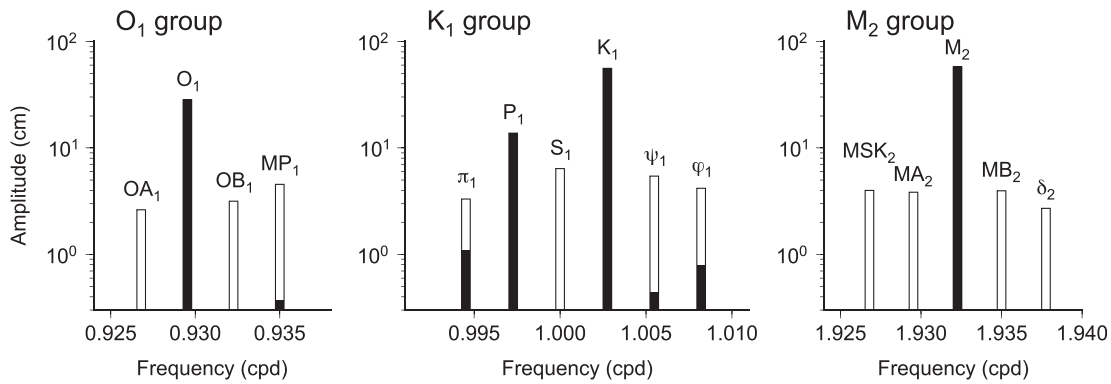
**Figure 8.** Observed amplitudes, in three main tidal groups, of the ocean tides at New Westminster, Canada, a location of an extraordinarily large $\psi_1$ constituent (amplitude 54 mm). Each constituent (vertical bar) is separated from its neighbor by 1 cpy in frequency. Nomenclature for $OA_1$, $OB_1$ follows that often used for the annual sidelines of $M_2$ (e.g. Amin 1982). Filled part of each vertical bar represents the linear part of that constituent (the linear constituent coinciding with the compound $MP_1$ is $\tau_1$). The presence of large annual sidelines in $O_1$ and $M_2$ suggests that much of the large $\psi_1$ tide (and also $\pi_1$ and $S_1$) similarly owes to seasonality of $K_1$ and $P_1$.
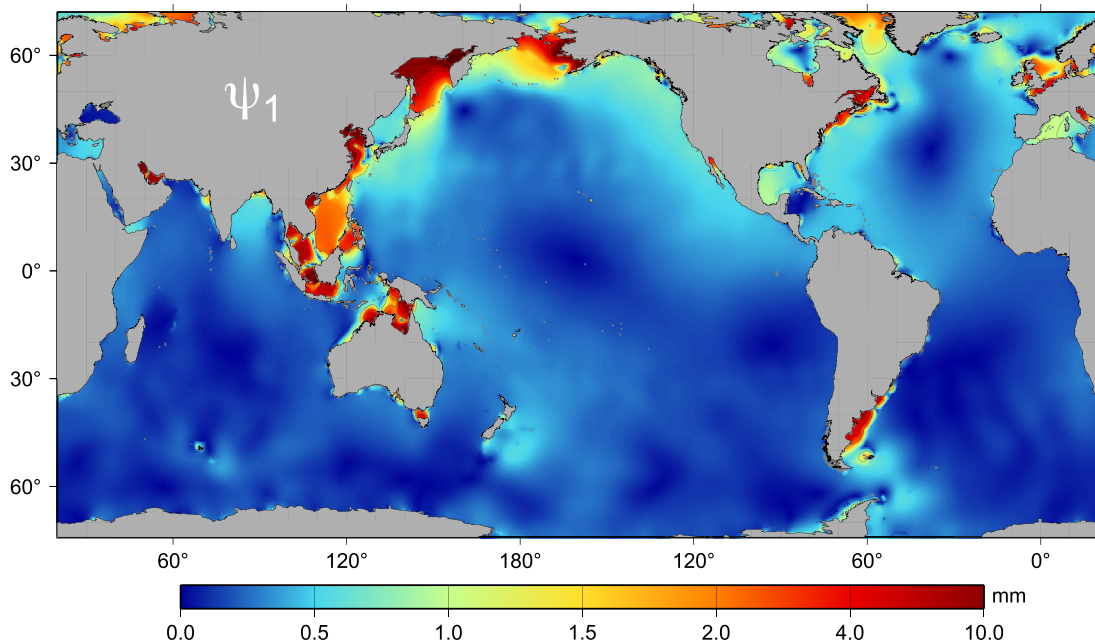


**Figure 9.** Amplitude of the $\psi_1$ tide caused by annual perturbations to $K_1$, according to a 5-yr HYCOM simulation. The simulation was forced by atmospheric winds and buoyancy fields, and by 8 pure harmonics of the tidal potential, *not* including $\psi_1$. Note non-linear colour scale. Contour lines are every 1 mm.

in part because of the many Atlantic stations. The gravitational part alone gives an RMS difference of 0.78 mm, which represents a reasonable reduction in variance, especially since the "truth" data in this case must have substantial errors of their own. Adding in the radiational component reduces this further to 0.73 mm.

The final line of Table 2, representing the full combined model, is more discouraging. The HYCOM component, representing the seasonal $K_1$ effect, is small throughout most of the deep ocean (Fig. 9), so its effect here is small, but it nonetheless slightly inflates the RMS difference. The tests suggest that in the deep, open ocean, the gravitational component is probably accurate, which is not surprising since it is inferred from the TPXO.8 atlas, and the radiational component appears reasonable. The HYCOM component, while encouraging in the East China Sea (Table 1) where amplitudes are substantial, appears less reliable in the low-amplitude deep ocean.

## 7 THE EFFECT ON TIDAL GRAVITY

As the expectation that the $\psi_1$ ocean tide can be important to the analysis of the FCN resonance formed the justification for this work, it is fitting to see if our preoccupation with this tiny constituent was warranted. This section therefore examines the contributions of our three primary components of $\psi_1$ to tidal gravity observations.

We here use a spherical harmonic series approach to evaluate efficiently the gravity effect over the entire globe (Merriam 1980). Conventional loading Love numbers were adopted from Farrell (1972). Fig. 11 displays the resulting gravimetric load tides for the three investigated components. For the radiational component we used the data shown in Fig. 7(b), which corresponds to the ocean's dynamic response to pressure loading and therefore complements the standard atmospheric correction to gravimetry which assumes an isostatic response (Boy 2019). Of the three components the gravitational is generally the largest, which is fortunate
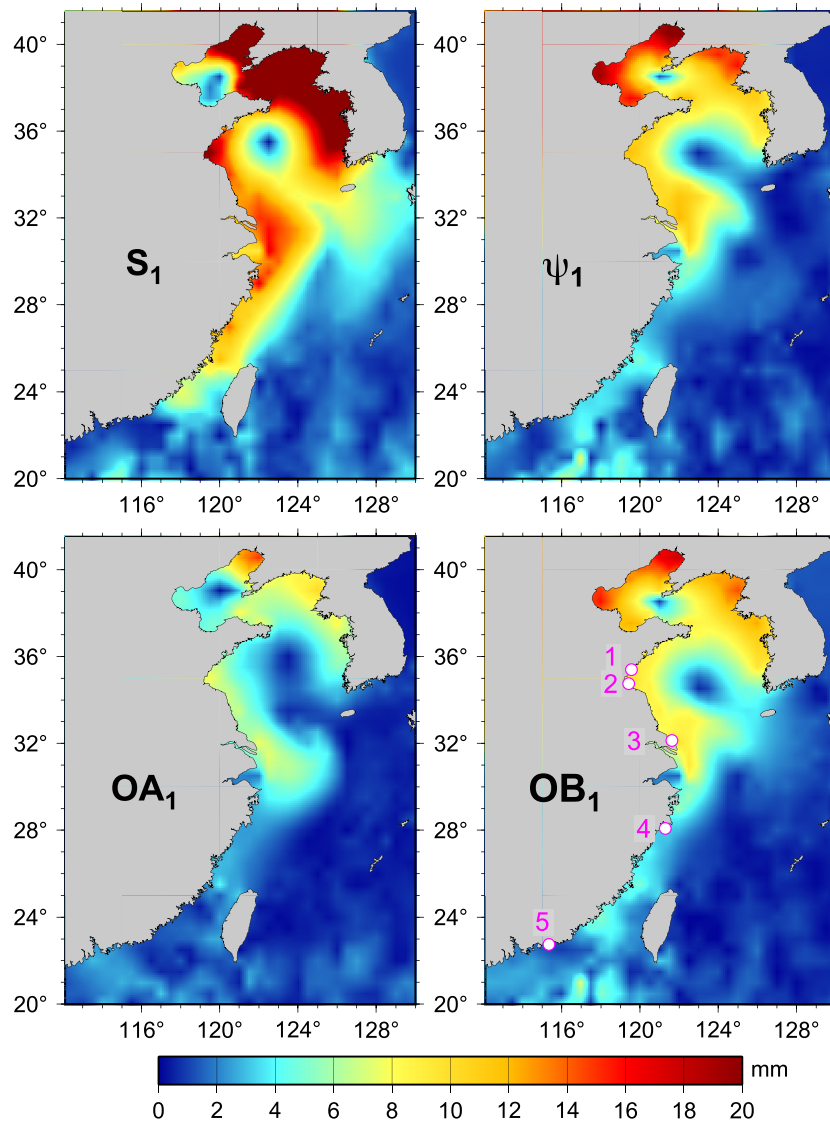
**Figure 10.** Amplitides of the two annual sidelines of $K_1$ (top panels) and $O_1$ (lower panels) according to our 5-yr HYCOM simulation. Results shown for constituent $OB_1$ (lower right) are compared in Table 1 against five tide gauges (white circles).

**Table 1.** Annual $O_1$ sideline: HYCOM versus tide gauges.

| Tide gauge | $OB_1$ amplitude (mm) | | $OB_1$ phase (°) | |
|---|---|---|---|---|
| | Gauge | HYCOM | Gauge | HYCOM |
| 1. Shijiusuo | 8.7 | 9.2 | 314° | 252° |
| 2. Lianyungang | 9.8 | 8.4 | 298° | 269° |
| 3. Lusi | 7.5 | 9.3 | 88° | 23° |
| 4. Kanmen | 5.7 | 2.8 | 111° | 105° |
| 5. Shanwei | 2.8 | 1.9 | 137° | 164° |

*Note*: Gauge numbers correspond to map labels on Fig. 10.

**Table 2.** RMS differences (mm) with 114 bottom pressure estimates of $\psi_1$. RMS signal is 1.15 mm.

| Model component(s) | RMS |
|---|---|
| Gravitational | 0.78 |
| Gravitational + radiational∗ | 0.73 |
| Gravitational + HYCOM + rad. | 0.78 |

∗The radiational component corresponds to Fig. 7b, so it includes the atmospheric tide.

since that component is probably the most accurate. However, in the western marginal seas of the Pacific and Atlantic, the seasonal $K_1$ component is often significantly larger. The radiational component is generally small, but it is still significant in the South China Sea and the northwest Indian Ocean.

One example suffices to establish the importance of these load-tide corrections to analyses of gravimetric earth tides. We examined the (relatively short) time series of measurements collected with a superconducting gravity meter at Hsinchu, Taiwan, between September 2006 and February 2008. The estimated amplitude of the $\psi_1$ tide is 3.5 nm s$^{-2}$, while theoretical gravity at that station is 2.648 nm s$^{-2}$ (rigid earth). Allowing for a non-rigid earth, with a gravimetric factor $\delta = (1 + h_2 - 3k_2/2)$ (Lambeck 1988), and using the Love numbers of Wahr (1981) versus those of Mathews *et al.* (1995) gives theoretical values of 3.279 versus 3.364 nm s$^{-2}$, respectively. Distinguishing among different earth models therefore requires a precision in the load tide well below 0.1 nm s$^{-2}$. For our three components (gravitational, radiational, and seasonal $K_1$)
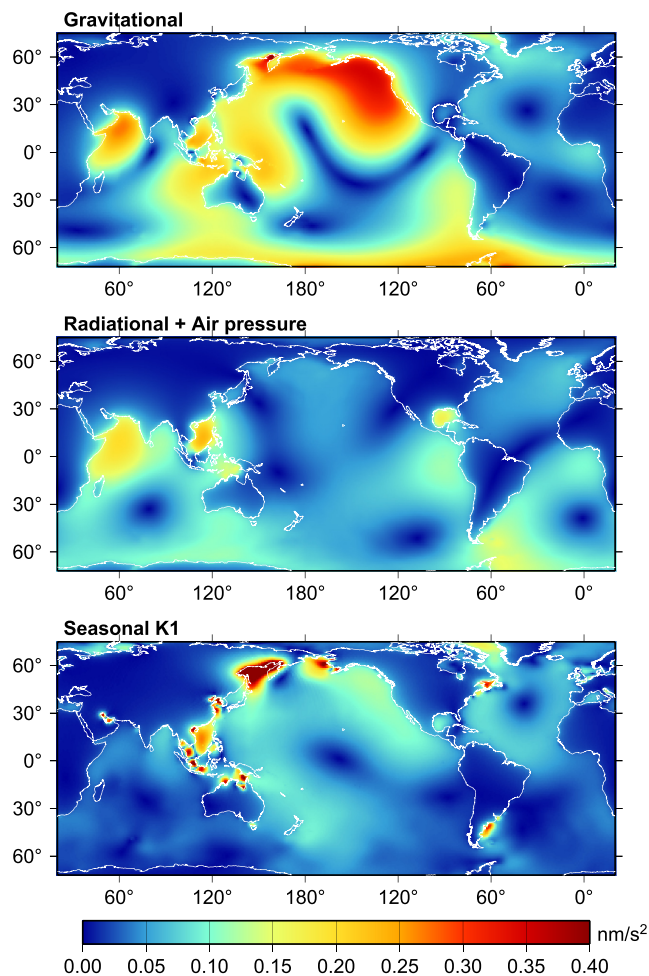
**Figure 11.** Gravimetric $\psi_1$ ocean tide loading amplitudes, for the three components of the ocean tide considered here: gravimetric, radiational and that part due to seasonal modulation of $K_1$. Units are nm s$^{-2}$ (or 0.1 $\mu$Gal).

evaluated at Hsinchu, we obtain 0.116, 0.109 and 0.128 nm s$^{-2}$, respectively. The magnitudes of these corrections thus suggests they are critical to any successful analysis of the $\psi_1$ earth tide at this or similar locations. Of course, a gravimeter located in the interior of a large continent is always much less affected by ocean tidal loading, and Fig. 11 acts as a useful guide to where such locations exist.

Incidentally, while computing the gravity effects of the $\psi_1$ ocean tide, we also computed the associated vertical and horizontal crustal deformations. The maximum amplitude, occurring near the tidal resonance in the upper Okhotsk Sea, is only 0.8 mm, and elsewhere the amplitudes are less than 0.2 mm.

## 8 CONCLUSIONS

A primary motivation of this work has been to outline the difficulties in developing a reliable model of the $\psi_1$ ocean tide. Previous studies of the NDFW based on gravimetry have been aware of the need to account for the core resonance when inferring $\psi_1$ from other diurnal ocean-tide models (e.g. Merriam 1994; Ducarme *et al.* 2007), but this gravitational component, as we have seen, is only part of the ocean's $\psi_1$ tide. A significant additional part is caused by seasonal variations in $K_1$, which, although small in the open ocean, are large

in some marginal seas, especially in the Western Pacific. The radiational part of $\psi_1$, arising from pressure loading by the atmospheric tide, is also important in some areas.

The radiational component of the $\psi_1$ ocean elevations is rather erratic, especially in high latitudes, owing to non-tidal atmospheric pressure variability in the diurnal band. However, much of this variability is high-wavenumber and is found to satisfy a nearly inverted-barometer response to the pressure field. Much of the 'noise' thus disappears in bottom pressure of the combined ocean plus atmospheric tide, but there is a clear dynamic response remaining (Fig. 7). The dynamic response will be overlooked with standard methods that correct geodetic data (e.g. gravimeters) for atmospheric mass variability while assuming an inverted-barometer ocean response.

The HYCOM simulation used here to study seasonality of the $K_1$ ocean tide was computed almost a decade ago (Shriver *et al.* 2012), and more extensive and realistic simulations of tides in the presence of ocean circulation variability have appeared in the meantime (e.g. Arbic *et al.* 2018). By good fortune, however, this particular multi-year simulation was ideal for our purposes, because its simple tidal spectrum had no energy at $\psi_1$ and it excluded atmospheric pressure forcing. This allowed us to explore these mechanisms separately to understand how each contributes to the actual $\psi_1$ ocean tide.

The initial models developed here represent some progress in understanding $\psi_1$ and in developing models needed by the geodetic community, although greater accuracies are needed. The work lays out some of the complex issues involved in modelling this small constituent. Given the difficulties associated with the non-gravitational components of $\psi_1$, we are still inclined to describe this ocean tide constituent as 'problematic'.

## DATA AVAILABILITY STATEMENT

The data underlying this paper are available in the article and in its online supplementary material. ECMWF ERA5 pressure data are available from the Copernicus Climate Change Service https://cds.climate.copernicus.eu. The Chinese tide gauge data used to construct Table 1 were downloaded from the archives of the University of Hawaii Sea Level Center. Data from the Hsinchu superconducting gravimeter are available from the International Geodynamics and Earth Tide Service.

# REFERENCES

Álvarez, O., Tejedor, B., Tejedor, L. & Kagan, B. A., 2003. A note on sea-breeze-induced seasonal variability in the $K_1$ tidal constants in Cádiz Bay, Spain, *Estuar. Coastal Shelf Sci.,* **58,** 805–812.

Amin, M., 1982. On analysis and prediction of tides on the west coast of Great Britain, *Geophys. J. R. astr. Soc.,* **68,** 57–78.

Arbic, B.K. *et al.*, 2018. A primer on global internal tide models and internal gravity wave continuum modeling in HYCOM and MITgcm, in *New Frontiers in Operational Oceanography,* pp. 307–391, eds Chassignet, E. *et al.*, GODAE OceanView.

Arbic, B.K., Wallcraft, A.J. & Metzger, E.J., 2010. Concurrent simulation of the eddying general circulation and tides in a global ocean model, *Ocean Model.,* **32,** 175–187.

Boy, J.-P., 2019. Description of the level 2 and level 3 IGETS data produced by EOST, *Int. Geodyn. Earth Tide Serv.,* https://isdc.gfz-potsdam.de/fileadmin/isdc/docs/EOSTproducts.pdf.

Carrère, L. & Lyard, F., 2003. Modeling the barotropic response of the global ocean to atmospheric wind and pressure forcing – comparisons with observations, *Geophys. Res. Lett.,* **30**(6), doi:10.1029/2002GL016473.

Carrère, L., Faugère, Y. & Ablain, M., 2016. Major improvement of altimetry sea level estimations using pressure-derived corrections based on ERA-Interim atmospheric reanalysis, *Ocean Sci.,* **12,** 825–842.

Cartwright, D.E., 1968. A unified analysis of tides and surges round north and east Britain, *Phil. Trans. R. Soc.,* **263**(1134), 1–55.

Cartwright, D.E. & Edden, A.C., 1973. Corrected tables of tidal harmonics, *Geophys. J. R. astr. Soc.,* **33,** 253–264.

Cartwright, D.E. & Tayler, R.J., 1971. New computations of the tide-generating potential, *Geophys. J. R. astr. Soc.,* **23,** 45–74.

Chao, B.F. & Hsieh, Y., 2015. The earth's free core nutation: Formulation of dynamics and estimation of eigenperiod from the very-long-baseline interferometry data, *Earth planet. Sci. Lett.,* **432,** 483–492.

Corkan, R.H., 1934. An annual perturbation in the range of tide, *Proc. R. Soc.,* **144,** 537–559.

Covey, C., Dai, A., Lindzen, R.S. & Marsh, D., 2014. Atmospheric tides in the latest generation of climate models, *J. Atmos. Sci.,* **71,** 1905–1913.

Cui, X., Sun, H., Xu, J., Zhou, J. & Chen, X., 2018. Detection of free core nutation resonance variation in earth tide from global superconducting gravimeter observations, *Earth Planet. Space.,* **70,** 199,.

Cummins, P.F., Masson, D. & Foreman, M.G.G., 2000. Stratification and mean flow effects on diurnal tidal currents off Vancouver Island, *J. Phys. Oceanogr.,* **30,** 15–30.

Dai, A. & Wang, J., 1999. Diurnal and semidiurnal tides in global surface pressure data, *J. Atmos. Sci.,* **56,** 3874–3891.

Dehant, V. & Mathews, P.M., 2015. *Precession, Nutation, and Wobble of the Earth,* Cambridge Univ. Press.

Ducarme, B., Sun, H.-P. & Xu, J.-Q., 2007. Determination of the free core nutation period from tidal gravity observations of the GGP superconducting gravimeter network, *J. Geod.,* **81,** 179–187.

Egbert, G.D. & Erofeeva, S.Y., 2002. Efficient inverse modeling of barotropic ocean tides, *J. Atmos. Oceanic Tech.,* **19,** 183–204.

Farrell, W.E., 1972. Deformation of the earth by surface loads, *Rev. Geophys. Space Phys.,* **10,** 761–797.

Gelaro, R. *et al.*, 2017. The modern-era retrospective analysis for research and applications, version 2 (MERRA-2), *J. Climate,* **30,** 5419–5454.

Greff-Lefftz, M. & Legros, H., 1999. Correlation between some major geological events and resonances between the free core nutation and luni-solar tidal waves, *Geophys. J. Int.,* **139,** 131–151.

Hamilton, K. & Garcia, R.R., 1986. Theory and observations of the short-period normal mode oscillations of the atmosphere, *J. geophys. Res.,* **91,** 11 867–11 875.

Herring, T.A., Gwinn, C.R. & Shapiro, I.I., 1986. Geodesy by radio interferometry: Studies of the forced nutations of the earth: 1. Data analysis, *J. geophys. Res.,* **91,** 4745–4754.

Hersbach, H. *et al.*, 2020. The ERA5 global reanalysis, *Quart. J. R. Met. Soc.,* **146,** 1999–2049.

Huess, V. & Andersen, O.B., 2001. Seasonal variation in the main tidal constituent from altimetry, *Geophys. Res. Lett.,* **28,** 567–570.

Kang, S.K., Foreman, M.G.G., Lie, H.-J., Lee, J.-H., Cherniawsky, J. & Yum, K.-D., 2002. , Two-layer tidal modeling of the Yellow and East China Seas with application to seasonal variability of the M2 tide, *J. geophys. Res.,* **107**(C3), 6–1-6-18.

Lambeck, K., 1988. *Geophysical Geodesy,* Clarendon Press.

Le Provost, C., 2001. Ocean tides, in *Satellite Altimetry and Earth Sciences: A Handbook of Techniques and Applications,* pp. 267–303, eds Fu, L.-L. & Cazenave, A., Academic Press.

Malin, S. R.C. & Chapman, S., 1970. Lunar tidal components $N_1$ and $O_2$ [sic] in the atmospheric pressure, *Pure appl. Geophys.,* **80,** 309–318.

Mathews, P.M., Buffett, B.A. & Shapiro, I.I., 1995. Love numbers for diurnal tides: relation to wobble admittances and resonance expansions, *J. geophys. Res.,* **100,** 9935–9948.

Mathews, P.M., Herring, T.A. & Buffett, B.A., 2002. Modeling of nutation and precession: new nutation series for nonrigid earth and insights into the earth's interior, *J. geophys. Res.,* **107,** 2068.

Matsuno, T., 1980. A trial of search for minor components of lunar tides and short period free oscillations of the atmosphere in surface pressure data, *J. Meteor. Soc. Jpn.,* **58,** 281–285.

Matthews, A.J. & Madden, R.A., 2000. Observed propagation and structure of the 33-h atmospheric Kelvin wave, *J. Atmos. Sci.,* **57,** 3488–3497.

Meeus, J., 1998. *Astronomical Algorithms,* 2nd edn., Willmann-Bell.

Merriam, J.B., 1980. The series computation of the gravitational perturbation due to an ocean tide, *Phys. Earth planet. Inter.,* **23,** 81–86.

Merriam, J.B., 1994. The nearly diurnal free wobble resonance in gravity measured at Cantley, Quebec, *Geophys. J. Int.,* **119,** 369–380.

Müller, M., 2009. *A Large Spectrum of Free Oscillations of the World Ocean includig the Full Ocean Loading and Self-attraction Effects,* Springer-Verlag.

Müller, M., Cherniawsky, J.Y., Foreman, M. G.G. & von Storch, J.-S., 2014. Seasonal variation of the M2 tide, *Ocean Dyn.,* **64**(2), 159–177.

Nelson, A.D., Arbic, B.K., Zaron, E.D., Savage, A.C., Richman, J.G., Buijsman, M.C. & Shriver, J.F., 2019. Toward realistic nonstationarity of semidiurnal baroclinic tides in a hydrodynamic model, *J. geophys. Res.,* **124,** 6632–6642.

Neuberg, J., Hinderer, J. & Zürn, W., 1987. Stacking gravity tide observations in central Europe for the retrieval of the complex eigenfrequency of the nearly diurnal wobble, *Geophys. J. R. astr. Soc.,* **91,** 853–868.

Percival, D.B. & Walden, A.T., 1993. *Spectral Analysis for Physical Applications,* Cambridge Univ. Press.

Ponte, R.M., Salstein, D.A. & Rosen, R.D., 1991. Sea level response to pressure forcing in a barotropic numerical model, *J. Phys. Oceanogr.,* **21,** 1043–1057.

Prinsenberg, S.J., 1988. Damping and phase advance of the tide in western Hudson Bay by the annual ice cover, *J. Phys. Oceanogr.,* **18,** 1744–1751.

Pugh, D.T. & Woodworth, P.L., 2014. *Sea Level Science: Understanding Tides, Surges, Tsunamis and Mean Sea-Level Changes,* Cambridge Univ. Press.

Ray, R.D., 2013. Precise comparisons of bottom-pressure and altimetric ocean tides, *J. geophys. Res.,* **118,** 4570–4584.

Ray, R.D., 2017. On tidal inference in the diurnal band, *J. Atmos. Oceanic Tech.,* **34,** 437–446.

Ray, R.D. & Egbert, G.D., 2004. The global $S_1$ tide, *J. Phys. Oceanogr.,* **34,** 1922–1935.

Ray, R.D. & Egbert, G.D., 2018. Tides and satellite altimetry, in *Satellite Altimetry over Oceans and Land Surfaces,* Chap. 13, pp. 427–458, eds Stammer, D. & Cazenave, A., CRC Press.

Rosat, S., Florsch, N., Hinderer, J. & Llubes, M., 2009. Estimation of the free core nutation parameters from SG data: sensitivity study and comparative analysis using linearized least squares and Bayesian methods, *J. Geodyn.,* **48,** 331–339.

Schindelegger, M. & Ray, R.D., 2014. Surface pressure tide climatologies deduced from a quality-controlled network of barometric observations, *Mon. Wea. Rev.,* **142,** 4872–4889.

Schindelegger, M., Salstein, D., Einspigel, D. & Mayerhofer, C., 2017. Diurnal atmosphere-ocean signals in earth's rotation rate and possible modulation through ENSO, *Geophys. Res. Lett.,* **44,** 2755–2762.

Shriver, J.F., Arbic, B.K., Richman, J.G., Ray, R.D., Metzger, E.J., Wallcraft, A.J. & Timko, P.G., 2012. An evaluation of the barotropic and internal tides in a high resolution global ocean circulation model, *J. geophys. Res.,* **117,** doi:10.1029/2012JC008170.

Stammer, D. *et al.*, 2014. Accuracy assessment of global barotropic ocean tide models, *Rev. Geophys.,* **52,** 243–282.

Toomre, A., 1974. On the 'nearly diurnal wobble' of the earth, *Geophys. J. R. astr. Soc.,* **38,** 335–348.

Vial, F., Lott, F. & Teitelbaum, H., 1994. A possible signal of the El Niño–Southern Oscillation in time series of the diurnal tide, *Geophys. Res. Lett.,* **21,** 1603–1606.

Wahr, J.M., 1981. Body tides on an elliptical, rotating, elastic and oceanless earth, *Geophys. J. R. astr. Soc.,* **64,** 677–704.

Wunsch, C., 1972. Bermuda sea level in relation to tides, weather, and baroclinic fluctuations, *Rev. Geophys. Space Phys.,* **10,** 1–49.

Wunsch, C. & Stammer, D., 1997. Atmospheric loading and the oceanic "inverted barometer" effect, *Rev. Geophys.,* **35,** 79–107.

Zwiers, F. & Hamilton, K., 1986. Simulation of solar tides in the Canadian Climate Centre general circulation model, *J. geophys. Res.,* **91,** 11 877–11 896.

## SUPPORTING INFORMATION

Supplementary data are available at *GJI* online.

**SupportingInfo.tar**
**Data set S1.** Global grid of $\psi_1$ amplitudes and phase lags.
**Data set S2.** Global grids of $\psi_1$ vertical and horizontal

Please note: Oxford University Press is not responsible for the content or functionality of any supporting materials supplied by the authors. Any queries (other than missing material) should be directed to the corresponding author for the paper.